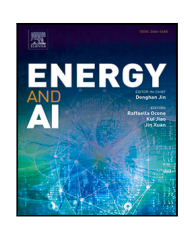
ELSEVIER

Contents lists available at ScienceDirect

Energy and AI

journal homepage: www.elsevier.com/locate/egyai





Effective thermal conductivity estimation using a convolutional neural network and its application in topology optimization

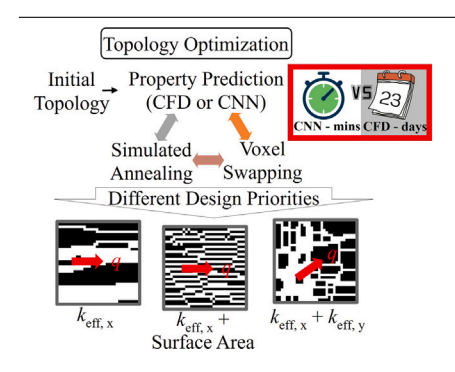
Andre Adam a, Huazhen Fang A, Xianglin Li a,b,*

- ^a Department of Mechanical Engineering, University of Kansas, 1530 W 15th St., Lawrence, 66045, KS, USA
- b Department of Mechanical Engineering and Materials Science, Washington University in St. Louis, One Brookings Drive, St. Louis, 63130, MO, USA

HIGHLIGHTS

- Dataset with 130,000 images and 520,000 effective thermal conductivity simulations
- CNN has MAPEs between 0.35% and 2.35% for ratios of thermal conductivity between 10 and 341.7.
- CNN predicts effective thermal conductivity in 15 ms on commercial GPU.
- Prediction speed is 20 ms on CPU for a single image.
- The CNN model is successful in 4 cases of topology optimization.

GRAPHICAL ABSTRACT



ARTICLE INFO

Keywords: Machine learning Effective thermal conductivity Convolutional neural network VGG

Numerical heat transfer Topology optimization

ABSTRACT

Topology optimization of heterogeneous structures can find significant use in a wide range of applications, and its fabrication has been made possible by recent advances in additive manufacturing. However, the optimization procedure is computationally expensive, as each structural update requires the re-evaluation of the properties. The computational time is the major limiting factor in large-scale and complex structural optimization. In this study, a convolutional neural network (CNN) model for predicting effective thermal conductivity inspired by the VGG networks is proposed. Trained using 130,000 unique binary images, the model achieves high predictive accuracy. Specifically, it shows a mean absolute percent error (MAPE) of 0.35% in testing when the thermal conductivity of the solid is ten times larger than the fluid, and when the thermal conductivities assigned are that of aluminum and water, the MAPE is 2.35%. The prediction time is 15 ms for a single image with 128×128 pixels, which is 3 to 5 orders of magnitude faster than a finite volume simulation. When employed in topology optimization, the CNN retains a MAPE between 0.67% and 11.8% for different cases. The CNN model correctly predicts trends in effective thermal conductivity and improves the structure to close proximity of a theoretical maximum in all cases.

E-mail address: lxianglin@wustl.edu (X. Li).

^{*} Corresponding author at: Department of Mechanical Engineering and Materials Science, Washington University in St. Louis, One Brookings Drive, St. Louis, 63130, MO, USA.

1. Introduction

Heterogeneous materials are an intrinsic aspect of many fields of study in science and engineering for their incredible inherent mechanical and transport properties [1]. In energy research, transport properties related to the geometry, orientation, and topology of the material are often intrinsic to overall system performance. Studies have shown several physical properties, such as effective diffusivity [2,3], permeability [2,4,5], or even structural properties [6], have integral dependence on the distribution of the phases involved.

One such property is the effective thermal conductivity [2,3], which refers to thermal conductivity when the convective and radiative heat transfer are negligible and at least two phases with different conducive properties are involved. This property has a wide range of applications, especially in porous media that impede general fluid flow and do not have significant temperature gradients across the structure, and is relevant across the fields of petroleum engineering, geology, electrochemistry, and food science, among others.

A multitude of analytical and empirical correlations have been made to predict the effective thermal conductivity of a system [7,8], but such models often assume simplified geometries, thus having very limited ranges of validity covering small subsets of topology and porosity. The alternative is experimenting or simulating to predict the property, both of which have significant physical time and cost associated. An alternative method for obtaining both effective thermal conductivity and effective diffusivity efficiently is based on the random-walk theory [8,9]. These studies highlight the speed advantage of random-walk-based models over conventional numercial heat transfer (NHT) models, while providing higher accuracy than empirical models. This type of model has the added benefit of providing fast computations for either 2D or 3D domains.

Recent progress in machine learning (ML) and computer vision have allowed to build data-driven predictive models that provide computational understanding of topological features. A convolutional neural network (CNN) is a particular type of neural network that was originally introduced as the "Neocognitron" [10], a computational model inspired by Hubel and Wiesel's hierarchical receptive field model of the visual cortex. Since then, a number of improvements have been made to the topic of image segmentation [11]. Particularly suitable for the implementation of CNNs is graphic processing units (GPUs), which have seen fast growth in their computing power and scalability in recent years.

Two recent studies [12,13] have successfully implemented CNN-based models for structure–property integration for materials science. These studies utilized the ability of convolutional layers to extract key features from a structure and feed them to fully connected layers to predict material properties. Through training, the model learns to extract crucial topological features and make an educated guess at the relevant physical feature from the extracted information.

In energy research, Wu et al. [14] considered CNN architectures based on AlexNet [15] and ResNet [16] to predict the effective diffusivity of porous media solely from images, with a training dataset of 1960 samples. The proposed model performs more accurately than empirical. However, the accuracy is still limited to a certain extent, possibly because of the relatively few images to train the CNN. The prediction time is not discussed, and there is no validation of the CNN model with data outside the dataset.

Wei et al. [17] used a CNN as well as other ML methods to predict the effective thermal conductivity of composite materials and porous media. With an original CNN architecture, using a maximum dataset size of 1400 samples, an accuracy in terms of correlation coefficient (R^2) of 0.986 or a relative mean squared error (RMSE) of 1.9% is reported, which is often more accurate than popular analytic models such as Maxwell-Eucken model or the Bruggeman model. Zhu et al. [18] proposes another CNN based model with original architecture, and for 300 samples on a 90/10 split between train/test dataset, the authors

display a R^2 value of 0.93 and a mean absolute error of 5.2 W/(m K) in testing. Other studies also compare different ML methods for predicting and optimizing thermal transport models [19], highlighting the effectiveness of such models in property prediction and their use in material optimization.

While the aforementioned studies [14,17,18] use CNNs for predicting properties relevant to energy research, the accuracy and efficiency need to be further refined in order to be employed in practical situations, as there are no discussions on prediction time, CNN optimization, and general predictions outside of the dataset. This study uses recent advancements in training CNNs and parameter optimization to propose a CNN-based model to predict effective thermal conductivity. We thoroughly discuss how the accuracy of the NHT model, CNN architecture, hyperparameter selection, dataset size, and training schedule all collectively impact the accuracy of the CNN in predicting effective thermal conductivity, while also taking in consideration the prediction speed. Finally, this CNN model is validated with structures that possess analytical results and data outside the dataset, to make sure the CNN model can retain accuracy in prediction even if the input is significantly different from the training dataset. Our model is optimized for speed, accuracy, and generalization across multiple types of 2D structures, by drawing inspiration from the VGG-class [20] networks. The CNN-based models can make predictions from newly entered data in milliseconds. In contrast, a prediction of a 3D model using the random-walk approach takes seconds [8,9], and a 3D NHT model takes minutes.

We created a dataset with more than 130,000 images and their thermal conductivities simulated by central-differencing based NHT model. The NHT model is parallelized and all NHT simulations were performed with the resources from the Bridges2 supercomputer from the Pittsburgh Supercomputing Center. The size of the dataset can be hard to manage on a conventional computer, so the training and testing of the proposed CNN models and architectures are all done with resources from the GPU partition of the Expanse supercomputer at the San Diego Supercomputer Center.

Another objective of the study is to assess whether or not the CNN predictive model can be applied to iterative topology optimization problems. Topology optimization is a process of changing structures to maximize or minimize a specific property [21]. The main challenge in iterative topology optimization is that the optimized properties of the structure must be reassessed at every structural update. Thus the computational cost often limits the size of the domain as well as the complexity of the model [22,23]. The CNN-based predictive model could reduce the computational time by orders of magnitude, enabling much larger domains as well as complex cost functions. The prediction accuracy of material properties at each step is critical to the success of topology optimization. Despite some existing studies on ML for material optimization [24], a CNN model that is accurate enough for iterative topology optimization has yet to be successfully demonstrated, to the best of the authors knowledge.

The following section will outline the dataset generation. Section 3 then presents the choice of architecture and hyperparameter optimization, which is an adaptation from the VGG [20] family of CNNs. Section 4 investigates the accuracy of the model in training and testing, potential sources of error, prediction speed in different environments, and validations of the proposed model using test cases from analytical solutions. Section 5 applies the trained CNN models to test four cases in topology optimization to demonstrate a practical application of the model. Section 6 concludes the work. The trained network, the training dataset [25], and a sample code showing how to load and use the models are available to download.

 $^{^{1}\,}$ GitHub to trained networks and sample code: https://github.com/adama-wzr/CNN-Keff

Fig. 1. One example from each generated dataset. (a) shows a structure of randomly packed circles. (b) is a sample of an ellipse-packed domain. (c) is an example of rectangle packing. (d) shows a sample image generated with the OSGS algorithm. All images have 128 × 128 pixels.

2. Training dataset generation

2.1. Image generation

A key component of this study is the generation of images for the training dataset, as well as simulating their effective thermal conductivity. Ideally, these images would encompass as many different types of heterogeneous structures as possible, such that the CNN model applies to a broad range of structures after training. Sharing the images in an open-access format encourages other researchers to contribute to this dataset, making it better generalized over time, and exposing the CNN in training to as many features as possible.

While there are several methods [26,27] to digitally reconstruct structures, most methods are constrained in speed and/or require digital image scans, analytical correlations, or detailed structure information. Since the goal is to compile the most general possible dataset, a stochastic approach is taken by packing a domain with regular structures of arbitrary sizes. Past research [28–30] has established some resemblance between randomly packed regular shapes with actual structures.

Four datasets are created for this study: random quadrilateral packing, random sphere packing, random ellipse packing, and quartet structure generation set (QSGS) [31], containing 10,000 images each. The random parameters of each dataset were established to provide a near-uniform distribution in effective thermal conductivity between the theoretical minimum and maximum. The dataset extensively covers the range of porosities and increases the odds of covering the full range of thermal conductivities. Fig. 1 displays a sample image from each dataset. Appendix A contains further details, such as porosity histograms and porosity versus effective thermal conductivity data.

For all the randomly-packed regular shapes, the number of objects is a uniform distribution between 1 and 30, the center of each individual object is also random, and the objects are allowed to overlap. In the random quadrilateral packing, the parameters controlling the images are the height and width, which are uniform distributions between 8 to 40 and 8 to 60 pixels, respectively. For the random circle packing, the radii follow an uniform distribution between 4 and 40 pixels. Finally, for the ellipse-packed structures, the semi-major axis varied between 10 and 30 pixels, and the semi-minor axis varied between 4 and 10 pixels, also follow uniform distributions. The 30,000 images generated this way represent simple yet realistic approximations of structures. The dataset can be further extended from the original images by rotating each by 90°, flipping the color scheme, and doing both, vielding 120,000 unique images. The 10,000 QSGS [31] images were created in two batches of 5000 with different parameters. For each subset of 5,000 images, the target solid volume fraction (P_s) varies between 0.1 and 0.9 uniformly, such that it starts at 0.1 and increases by 0.04 every 250 images. For the first subset, the seed probability, C_d , was set at 0.0025 for each voxel, which on a 128² domain yields approximately 40 particle seeds. The growth probability of each particle per iteration in the diagonals of a solid pixel, D_{diag} , is set to 0.0001, and the probability of growth on sides, D_{sides} , is set to 0.0004. For the second subset of images, C_d is set to 0.00125, yielding 20 particle seeds per domain, and

the rate of growth for the particles in each iteration is set to 0.0005 in the diagonals and 0.001 on the sides. The QSGS dataset is highly stochastic, so the 10,000 QSGS are not modified by rotating or flipping the color scheme. Our dataset includes 130,000 total binary images, each with the size of 128×128 pixels, to train the CNN.

2.2. NHT model

The efficiency and accuracy of the NHT model are paramount to the CNN dataset creation and training. Wu et al. [14] used 1,960 pairs of structures and effective diffusivity, Wei et al. [18] had 300 samples in the training dataset for effective thermal conductivity prediction. Those studies used the lattice Boltzmann method (LBM) and cited issues with computational time as a limiting factor. Hence, here we propose and validate a simple NHT model with well-established ranges of validity and high efficiency. This study focuses on 2D heat conduction problems, thus, the goal is to solve the 2D steady-state heat equation, shown in Eq. (1).

$$\frac{\partial}{\partial x} \left(k \frac{\partial T}{\partial x} \right) + \frac{\partial}{\partial y} \left(k \frac{\partial T}{\partial y} \right) = 0, \tag{1}$$

where k is the local thermal conductivity.

The second-order partial differential equation is discretized using a central differencing scheme. This model uses each pixel of the image as a control volume, so for a 128×128 image, the computational domain includes 128×128 cells. The temperatures are calculated at the center of the cells by the finite volume method. These approximations are verified using well-known heat transfer cases in Table 1 by gathering results from the NHT model and comparing them with the analytic solutions.

Eq. (1) can be generalized by defining non-dimensional parameters. A non-dimensional temperature, θ , is defined in Eq. (2) below.

$$\theta = \frac{T - T_{\text{cold}}}{T_{\text{hot}} - T_{\text{cold}}},\tag{2}$$

where T_{cold} and T_{hot} are the temperatures of the cold and hot sides of the domain. Dimensionless length scales can be defined as in Eq. (3), as functions of the height of the domain, H, and the width of the domain, W.

$$\xi = \frac{x}{W}$$

$$\eta = \frac{y}{H}$$
(3)

 $ar{k}$ is the non-dimensionalized thermal conductivity calculated by dividing the thermal conductivity of solid with the thermal conductivity of the fluid, as shown in Eq. (4). With this approach, the dimensionless effective thermal conductivity, $ar{k}_{\rm eff}$, is a measure of how much the solid contributes to the thermal conductivity of the system. The lowest possible value of $ar{k}_{\rm eff}$ is 1, which represents a domain filled with fluid. Likewise, the maximum possible value is $ar{k}_{\rm eff} = ar{k}_{\rm s}$, for a domain with

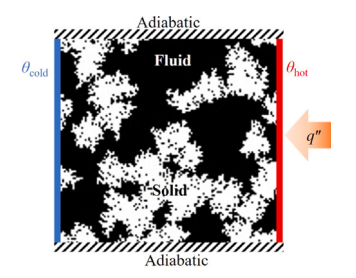


Fig. 2. Simulation domain with boundary conditions.

no fluid phase.

$$\bar{k}_{s} = \frac{k_{s}}{k_{f}}$$

$$\bar{k}_{f} = \frac{k_{f}}{k_{f}} = 1$$

$$\bar{k}_{eff} = \frac{k_{eff}}{k_{c}}$$
(4)

Thus, the steady-state dimensionless heat equation is shown Eq. (5)

$$\frac{\partial}{\partial \xi} \left(\bar{k} \frac{\partial \theta}{\partial \xi} \right) + \frac{\partial}{\partial \eta} \left(\bar{k} \frac{\partial \theta}{\partial \eta} \right) = 0 \tag{5}$$

This model setup yields a uniform structured mesh, meaning each control volume size $\Delta \xi = \Delta \eta$, which further simplifies the finite volume scheme. It is convenient to adopt the East, West, North, and South convention for i+1, i-1, j+1, and j-1, respectively. For the central location i,j, we adopt the letter P. It is also important to note that all heat fluxes are calculated at the interfaces between two adjacent cells, hence the thermal conductivity k used in the interface is the harmonic average between the two thermal conductivities.

We use the lowercase east, west, north, and south notation for the interface between cells. Since all cells have the same size, the harmonic mean for \bar{k}_w at the west interface of the central cell can be calculated using Eq. (6) below

$$\bar{k}_{\rm W} = \frac{2 \cdot \bar{k}_{\rm W} \bar{k}_{\rm P}}{\bar{k}_{\rm W} + \bar{k}_{\rm P}},\tag{6}$$

and the thermal conductivities at the other interfaces are calculated likewise.

The dimensionless temperature $\theta_{\rm hot}$ is set to 1 and $\theta_{\rm cold}$ is set to 0. Those are the constant temperature boundaries enforced on the right and left of the domain, respectively. The top and bottom boundaries are adiabatic. The arrow q'' simply indicates the direction of heat flux, and there are no heat injections from the exterior. This setup is shown in Fig. 2.

From the boundary conditions, it is clear that the heat flux should be the same across any vertical slice for a converged solution. The heat flux across the left boundary is defined as q_1'' , the heat flux across the right boundary is defined as q_r'' , and since the heat flux is supposed to be constant, $q_1'' - q_r''$ is chosen as the convergence criteria for the simulation. An example of how to calculate q_1'' for n cells at the left boundary is shown in Eq. (7).

$$q_{l}^{"} = \frac{1}{n} \sum_{i=1}^{n} \bar{k}_{i} \frac{\theta_{i} - \theta_{\text{cold}}}{\frac{\Delta \xi}{2}}$$
 (7)

where θ_i is the dimensionless temperature at each of the n cells adjacent to the left boundary. Similarly, the heat flux at the right boundary can be calculated as in Eq. (8).

$$q_{\rm r}^{\prime\prime} = \frac{1}{n} \sum_{i=1}^{n} \bar{k}_i \frac{\theta_{\rm hot} - \theta_i}{\frac{\Delta \xi}{2}} \tag{8}$$

where in this case θ_i is the dimensionless temperature at each of the n cells adjacent to the right boundary. Finally, since q_1'' and q_r'' should be

Table 1 Statistics showing the effect of increasing the \bar{k}_s on the performance and convergence of the NHT simulations.

\bar{k}_{s}	Avg. iterations	Avg. $ q_{\rm r}^{''} + q_{\rm l}^{''} $	Avg. Time (s)
10	32,903	$4.22 \cdot 10^{-8}$	34.2
50	72,350	$1.91 \cdot 10^{-7}$	81.6
100	105,096	$1.00 \cdot 10^{-6}$	137.3
341.7	154,307	$9.75 \cdot 10^{-5}$	371.2

the same from the simulation setup, it is convenient to define $q_{\rm avg}^{\prime\prime}$ as in Eq. (9).

$$q_{\rm avg}'' = \frac{q_{\rm r}'' + q_{\rm l}''}{2} \tag{9}$$

The dimensionless effective thermal conductivity can be calculated from Eq. (10).

$$\bar{k}_{\text{eff}} = \frac{q_{\text{avg}}''\xi}{(\theta_{\text{hot}} - \theta_{\text{cold}})} \tag{10}$$

2.3. NHT solution and details

This study used the tridiagonal matrix algorithm (TDMA) iteratively to maximize the efficiency of both memory storage and computational time. The TDMA approach deals with the three-diagonal system of linear equations. In testing, the iterative TDMA was 40% faster than the Jacobi iteration using the same convergence criteria.

There are two options in terms of parallel algorithms to increase speed. The first is to implement a parallel solver, which would involve using more computer cores to speed up each iteration. The second option is to simply have separate computing cores working on different images and only sharing the results amongst each other. The second option requires a scheme to coordinate the load balancing between cores, which is naturally much more efficient and simple than the first option. Therefore, the NHT model was implemented in C code, using OpenMP for the load balancing. Table 1 summarizes the relevant practical statistics from the NHT model. Note that the convergence speed and accuracy heavily depends on the ratio of thermal conductivities of the solid and fluid phases as well as the overall connectivity of the solid phase. When the conductivity ratio between the solid and fluid is 10, the NHT simulation per image per computer core takes 34.2 s on average. When the ratio of solid and fluid thermal conductivities is 341.7, the NHT simulations of the same images averaged over 370 s per image per core. The same model was also evaluated for \bar{k}_s of 50 and 100. Since each dataset has 130,000 images, a total of 520,000 2D cases were simulated and used for CNN training.

2.4. NHT validation

Parallel and series-arranged structures are used to validate the NHT simulations, as the theoretical solution arises from thermal resistance models [8]. $\bar{k}_{\rm eff}$ is a function of the thermal conductivity of solid and fluid phases, $\bar{k}_{\rm s}$ and $\bar{k}_{\rm f}$, as well as the porosity, ϵ . The theoretical values are calculated as follows:

series:
$$\bar{k}_{\text{eff}} = \left(\frac{\epsilon}{\bar{k}_{\text{f}}} + \frac{1 - \epsilon}{\bar{k}_{\text{s}}}\right)^{-1}$$
 (11)

parallel:
$$\bar{k}_{eff} = \epsilon \cdot \bar{k}_f + (1 - \epsilon) \cdot \bar{k}_s$$
 (12)

In the NHT simulations, the 128×128 images for the parallel and series structures were generated for five different porosities. Seven different ratios of $\bar{k}_{\rm S}$ were simulated. The results are benchmarked versus the analytical relations in Eqs. (11) and (12) are displayed in Fig. 3.

The largest relative error from any NHT result compared to the theoretical from Eq. (12) for the parallel case is in the order of 10^{-7} .

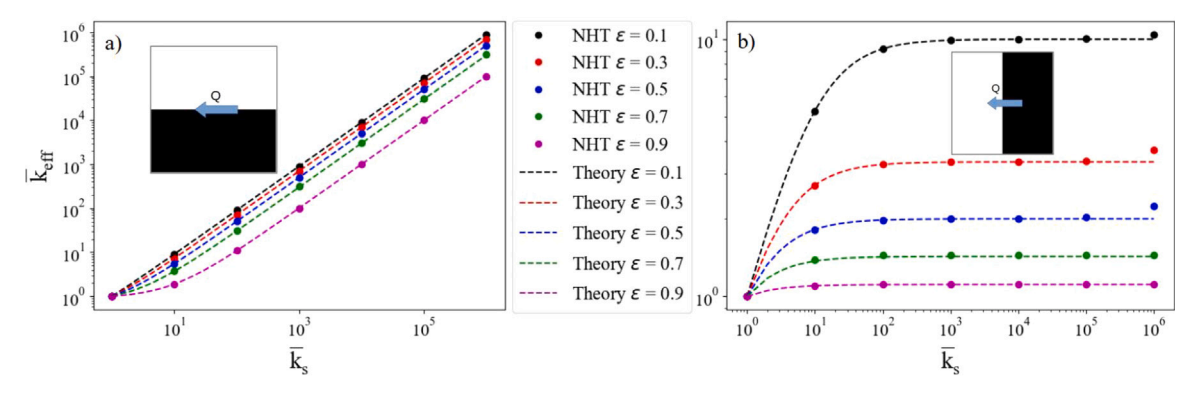


Fig. 3. Theoretical results versus the NHT model. The parallel arrangement results are on the left, and the series arrangement results are on the right.

However, upon inspection of Fig. 3, it is clear that there is a much larger relative error for the series case. The validation shows that the lower the conductivity ratio, the less error is introduced. For a porosity of 0.1, the relative error reaches a maximum of 4.5%, when the thermal conductivity ratio is 10^6 . Introducing such errors into the training of the CNN can be detrimental to the CNNs predictive ability. Hence the ratio of thermal conductivities is kept below 10^4 for the remainder of the study. As the conductivity gradients are more moderate, the central difference algorithm is good for discretizing the governing equation. The coefficient matrix from the NHT model has a lower condition number when the conductivity ratio is approaching 1, which is also evident from the accuracies displayed in Table 1.

In Appendix B the accuracy of the finite volume method is compared with two other studies [32,33]. These studies employed analogous theoretical test cases to assess the precision of the LBM.

3. CNN selection & optimization

A multitude of CNNs are available for the problem of image segmentation and detection. For the problem of predicting physical properties based on geometry, the ideal network provides a combination of sufficient accuracy with a reasonable computational cost. The VGGclass [20] networks, namely VGG16 and 19, are peculiar in the way the layers are stacked, having some unique advantages that are particularly relevant in terms of efficiency, memory storage, and training speed. The VGG networks only use 3×3 filters in the convolutional layers with a stride of 1. The 3×3 filter is the smallest filter that can distinguish up. down, left, and right. An effective receptive field is created by stacking multiple layers of 3×3 filters before a max pooling operation. As an example, if two 3 × 3 layers are stacked, an effective receptive field of 5×5 is created. As explained in the original manuscript for the VGG network [20], the main advantage of this practice is the efficiency of the network: a four-layer stack of 3 × 3 filters has an effective field of view of 9 \times 9, while only storing and training $4(3^2C^2)$ parameters, where C is the number of channels. In total, that is $36C^2$ parameters. On the other hand, a regular layer with a 9 \times 9 filter has 9^2C^2 or $81C^2$ parameters, which requires 125% more parameters for the same effective field of view.

Other than architectural advantages, selecting appropriate hyperparameters for the chosen network is an essential step that often requires a lot of trials and a general understanding of machine learning techniques and algorithms [34]. For this section, since the optimization process involves an extensive trial of the network, a subset of the dataset containing only the original 30,000 regular shape-packed images is employed, thus reducing computational time and allowing for a deep and extensive search for ideal architecture and hyperparameters. The ratio of thermal conductivities used is set to 10 to minimize the computational error and computational time of the NHT model. The objective of the study is to tackle ambiguities in the prior art and justify the selection of general hyperparameters for problems that focus on

Table 2

Effect of number of convolutional layers on training and validation accuracy.

Conv layers	MAPE Training	MAPE Test
2	1.11%	4.27%
4	1.18%	4.04%
6	0.96%	2.58%
8	1.09%	2.53%
12	0.92%	1.09%
16	0.93%	0.90%

effective thermal conductivity. The loss function is the mean absolute percent error (MAPE) function from the Keras API. For n samples, the equation to calculate MAPE is shown in Eq. (13).

MAPE =
$$\frac{100\%}{n} \sum_{i=1}^{n} \frac{|Y_{\text{true}}^{i} - Y_{\text{pred}}^{i}|}{Y_{\text{true}}^{i}}$$
 (13)

3.1. CNN architecture optimization

The VGG network and most other networks used in literature are designed to excel at image classification tasks. The scope of this work is to predict physical properties using the extracted feature maps. Hence this study uses $128 \times 128 \times 1$ binary images as the input as opposed to $224 \times 224 \times 3$ RGB images used in the original VGG-network. Other adaptations to the network must also follow to optimize it for the tasks of predicting effective thermal conductivity. Wu et al. [14] conclude from their work that the mean-squared error (MSE) trends to be smaller when the CNN has fewer convolutional layers. Similarly, Zhu et al. [18] arrived at a similar conclusion: the best accuracies in training and testing for effective thermal conductivity prediction were achieved when the CNN had 2 convolutional layers. Conversely, others [20,35] suggest that deeper networks are more capable of extracting relevant features. The deepest layers, as well as the fully-connected (FC) layers play a major role in the accuracy of prediction [36].

In this study, the number of nodes is increased from 2/2/1 to 128/128/1 in the FC layers to compare which architecture has the highest accuracy in testing and training. All convolutional layers and FC layers have the rectified linear unit (ReLU) activation function. The training is performed in 60 epochs with the Adam optimizer learning rate of $\lambda = 0.001$ and the batch size of 32. The training uses the same 80/20 train/test split for the trials shown in Table 2 while holding the 3 FC layers constant. The first two FCs have 64 nodes, and the last FC has one node as the model output.

The architecture with 16 convolutional layers looks the same as VGG19, which has 16 convolutional layers and 3 FC layers. Based on the trend in test MAPE displayed in Table 2, the more information is encoded through the convolutional layers, the more accurate the predictions in testing get. It is clear that overfitting is more prominent with fewer convolutional layers when the VGG-inspired network is used

Fig. 4. Architecture compiling the results from this section outlining the best performing network.

Table 3

Effect of number of FC nodes on training accuracy, validation accuracy, and number of parameters.

FC Nodes	MAPE Training	MAPE Test	Trainable parameters
2/2/1	44.68%	44.65%	321,809
4/4/1	1.07%	0.96%	317,653
8/8/1	1.04%	0.90%	321,587
16/16/1	1.00%	0.86%	330,217
32/32/1	1.15%	0.85%	347,417
64/64/1	0.99%	0.93%	383,353
128/128/1	0.99%	1.09%	461,369

for problems focusing on the effective thermal conductivity. Hence, the remainder of this study uses 16 convolutional layers, as displayed in Fig. 4.

Another aspect we considered is the number of nodes on the FC layers. In this architecture, the convolutional layers' job is to extract useful features to predict the relevant physical property. The FC layers' job is to make the actual prediction. With too many nodes in the FC layers, the network tends to overfit regardless of the convolutional layers' architecture. On the contrary, the network will be inaccurate without enough nodes. Additionally, the number of nodes of the FC layers heavily influences the number of trainable parameters in the network, which influences the training efficiency, memory storage, and prediction speed. We analyze the number of nodes on each FC layer using a process similar to the one used to determine convolutional layer design. Originally, the VGG19 for the classification problem with 1000 possible outputs has 4096/4096/1000 nodes on the fully connected layers. Those numbers are not suitable for this project. For example, we only need one output in the third layer. While keeping all training parameters the same as the study on the number of convolutional layers, we changed the numbers of nodes in the FC layers. Results are laid out in Table 3.

The number of nodes does not seem to have a big effect on the prediction accuracy as long as the number exceeds a minimum number. When the numbers of nodes are as small as 2/2/1, the prediction is highly inaccurate. When the numbers of nodes increase to 4/4/1 and to 64/64/1, all testing and training results have reasonable accuracy. We adopt 64/64/1 as it provides more consistency between testing and training accuracy while reserving sufficient nodes to tackle more complex problems but at the cost of having 20% more parameters than 4/4/1. Once the numbers of nodes are increased to 128/128/1, we observed slight trends towards overfitting.

Finally, the last aspects of the network's architecture that could be optimized are the grouping of the convolutional layers. After testing a few combinations of the number of channels, we find that the number of channels per convolutional layer does not significantly impact the accuracy. We adopt the configuration shown in Fig. 4 in order to balance the number of parameters. CNNs for classification problems use the *softmax* function in the last layer. But this study focuses on property prediction and uses a simple linear activation function in the last layer.

Table 4
Training outline and accuracy for selected combinations of parameters, all using 30,000 images.

Model	Batch Size	Learning Rate	Epochs	MAPE Train	MAPE Test
A	32	10^{-4}	600	0.52%	0.51%
В	32	10^{-4}	1600	0.28%	0.53%
C	64	10^{-4}	600	0.37%	0.85%
D	32	10^{-5}	2000	0.33%	0.77%

3.2. CNN training

The training of a CNN is a sensitive process that plays an intrinsic role in the ability of the model to extrapolate from training data to new data. A variety of methods are available, some of which include different mechanisms for decaying the learning rate as a function of the training epoch. Some recent studies suggest that instead of decreasing the learning rate, increasing the batch size is preferred [37]. We used the Adam [38] optimizer, which is notable for automatically handling learning rate decays. Hence the entered learning rate serves only as an upper limit, which in turn facilitates the optimization process by removing the momentum-related parameters.

This study has considered a wide range of learning rates, number of epochs, and batch sizes. But this section only highlights some combinations to display how specific parameters affect the accuracy and justify the final decision on which schedule to use. All of them were used to train the network shown in Fig. 4. Table 4 outlines the parameters of 4 different training schedules with the accompanying MAPEs in training and testing for our network.

Model A presents the best consistency between training and validation, does not overfit, and oscillates the least in later epochs. Model B performs better in training than in testing, which indicates a certain degree of overfitting. Model B is the one outlined in prior art [14] for the problem of effective diffusivity. When model B is applied to the current problem, the number of epochs is excessive and does not provide any benefits in testing compared to model A. On the other hand, increasing the batch size for model C only results in more overfitting and higher MAPE compared to the similar Model A. Increasing the batch size from Model A creates more overfitting, while decreasing batch size did not provide any benefits. Finally, lowering the learning rate and training for longer in model D does not improve the overall MAPE and generates the most overfitting. However, we note that model D considerably decreases MAPE oscillations in later epochs when compared to the other models. A more general and diverse dataset would neutralize the oscillations observed in models A, B, and C.

4. Results

4.1. Accuracy in training and testing

This subsection uses the entire 130,000 images in the dataset and considers four values of \bar{k}_s : 10, 50, 100, and 341.7. The ratio of 341.7

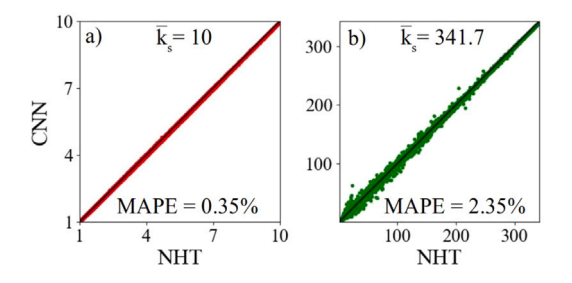


Fig. 5. CNN predictions versus NHT model effective thermal conductivity for the 26,000 images on the testing dataset. (a) predictions from the model using \bar{k}_s of 10. (b) predictions on the model trained with an aluminum-water combination.

Table 5 Statistics showing the effect of increasing the \bar{k}_s on the accuracy of the CNN prediction in training and testing.

\bar{k}_{s}	MAPE Train	MAPE Test
10	0.25%	0.35%
50	0.53%	1.08%
100	0.61%	1.74%
341.7	0.76%	2.35%

represents an aluminum-water system. All cases split 80% of the data for training and 20% for testing using the parameters for model A (Table 4). Fig. 5 compares between CNN-predicted results versus the NHT-simulated results of each of the 26,000 images in the testing dataset for the conductivity ratios of 10 and 341.7. Each CNN model was trained with 104,000 training data.

The visual inspection of Fig. 5 shows that the prediction errors increase for (b), with a higher \bar{k}_s . For the four ratios considered, Table 5 outlines the MAPEs and confirms the trend in decreasing accuracy with increasing thermal conductivity ratio. Section 2.4 and Table 1 also show increasing errors in NHT simulation as the thermal conductivity ratios increase, hence the result displayed in Fig. 5 and Table 5 hints at the error in CNN being a reflection and amplification of error introduced from NHT simulations. Also, note that the results outlined in Table 5 are for the model presented in Fig. 4 along with training scheme A from Table 4, with the only difference that the full dataset was employed in this section as opposed to the 30,000 images employed in Section 3. With the addition of the full dataset to the training process, the MAPE of the lowest thermal conductivity ratio dropped from 0.51% to 0.35% in testing.

4.2. Performance

Regardless of the thermal conductivity ratio, the batch CNN prediction time per batch is about 4 ms on a node with 4 NVIDIA V100 GPUs in the Expanse supercomputer. The CNN prediction time on an off-the-shelf NVIDIA GeForce RTX3070 is in the order of 15 ms. On a single CPU core, the CNN prediction time is about 20 ms when using a 3.6 GHz AMD Ryzen 7 3700X CPU. With the average NHT times reported in Table 1, using one CPU core, the CNN is 3 to 5 orders of magnitude faster than the NHT code.

The training of the CNN model takes around an hour to load the data and run 600 epochs on one HPC node with 4 NVIDIA V100 GPUs. We did not evaluate this process on a regular office computer due to constraints in RAM when loading the entire dataset.

4.3. Validation in theoretical cases

The same test cases used in Section 2.4 can be fed into the CNNs trained for the four values of $\bar{k}_{\rm s}$. The results are benchmarked versus theoretical solutions from Eqs. (11) and (12), and shown in Fig. 6.

When the conductivity ratio is 10, the MAPE is 0.44% for the parallel case and 1.61% for the series case. When the aluminum-water

system is simulated, the MAPE is 0.72% for the parallel case, and 1.57% for the series case. These results are consistent with trends observed in the previous subsection: larger errors (more than twice the MAPE) are observed when the effective properties approach that of the fluid phase. When the conductivity ratio is 10, the MAPE of the predictions is larger than the MAPE in testing shown in Table 5. But for the aluminum-water case, the MAPE of the predictions remains well below that in Table 5 for test. Finally, notice how the error for lower porosity presented in Fig. 6(b) resembles the error from Fig. 3(b), further evidence to support that the NHT accuracy is intrinsic to the CNN accuracy.

5. CNN-aided topology optimization

While there are several topology optimization approaches, this study simplifies the process to swapping voxels in the solid phase for voxels in the fluid phase. The objectives of this section are twofold: demonstrating that the CNN can present reasonable accuracy in realworld scenarios involving data outside of the training dataset, as well showing a potential application of the CNN in non-gradient iterative topology optimization as an efficient alternative to a conventional simulated physical property prediction. Thus, the focus is not on devising a unique optimization scheme, instead, the focus is on assessing the accuracy and efficiency of the CNN in different scenarios. The only restriction when picking the voxels for swapping is to pick voxels at the interfaces between the solid and fluid phases. In other words, the randomly selected voxel must have at least one adjacent voxel belonging to a different phase. During each iteration, if the voxel swap results in higher thermal conductivity or cost function, the swap is accepted. Otherwise, the two picked voxels will be returned to their original coordinates.

The simple voxel swapping approach can have large amounts of noise, thus taking millions, if not billions of iterations to converge [29]. A simple example employing a CNN on a 128 \times 128 voxel domain yielded more than 16,000 successful swaps. The $\bar{k}_{\rm eff}$ converged to within 10% of the theoretical maximum. We chose to bundle 4 \times 4 pixels together during the swap to save computational time.

The aforementioned process of random voxel swapping can lead to local maxima, where the thermal conductivity is not close to the theoretical maximum and yet no successful swaps can be found. For that reason, the simulated annealing algorithm (SAA) [39] is employed to determine if mutations occur or not. If the value of the cost function decrease, either the swap is reverted or a mutation occurs. Mutations are swaps that, albeit counterproductive to the optimization process from the point of view of the cost function, get accepted to avoid local minima/maxima. We applied the CNN model and SAA for one million iterations on a 32 × 32 domain of voxels with a porosity of 0.5 as an example. We showcase four optimization cases: maximizing the thermal conductivity in the x-direction with a thermal conductivity ratio of 10; maximizing the thermal conductivity of the aluminumwater combination with a conductivity ratio of 341.7 in the x-direction; optimizing the heat conduction in both x and y directions simultaneously with a thermal conductivity ratio of 10; and optimizing the thermal conductivity in the x-direction while also maximizing surface area. The initial phase configuration for all cases is the two phases connected in series, which has the lowest theoretical effective thermal conduction in the x-direction and the theoretical maximum in the y-direction.

The major benefit of CNN over NHT simulation is the prediction speed. From the benchmarks in Section 4.2, an aluminum-water NHT simulation would take, on average, 370 s per iteration. That would require around 102,778 h to attempt one million voxel swaps in topology optimization. In comparison, CNN completed one million topology optimization iterations on a commercial NVIDIA GEFORCE RTX 3070 in four and a half hours, with an average prediction speed of 15 ms per iteration.

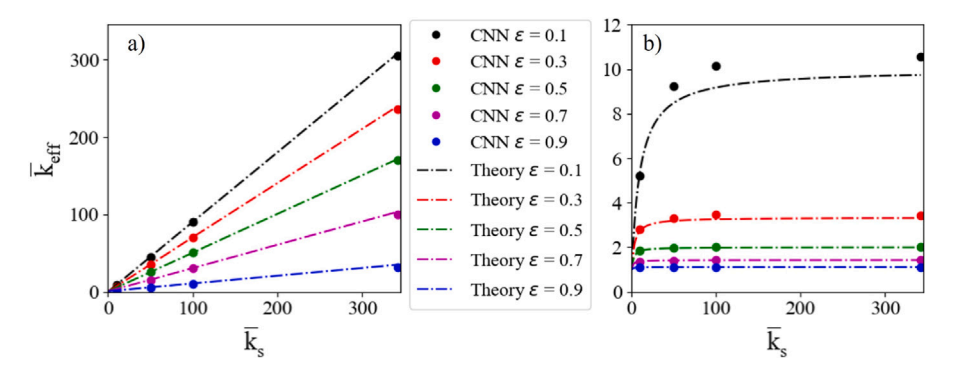


Fig. 6. Theoretical results versus the CNN model. (a) Parallel configuration cases are on the left. (b) Series configuration results.

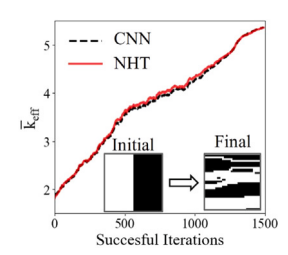


Fig. 7. Evolution of the $\bar{k}_{\rm eff}$ from topology optimization, comparing the NHT and CNN predictions for every step, as well as the evolution from initial to final structure.

5.1. Case A: k_{eff} in the x-direction, $\bar{k}_s = 10$

Within the one million swaps attempted, 1490 were deemed successful by CNN, and 911 mutations (not shown in Fig. 7) occurred in which the swaps were accepted. Fig. 7 shows the final result of the topology optimization, which starts from a theoretical worse case scenario. The final structure has a $\bar{k}_{\rm eff}$ of 5.36 according to the NHT model, which is 2.58% lower from the theoretical maximum of 5.5 calculated from Eq. (12). The CNN algorithm predicts the final structure has a $\bar{k}_{\rm eff}$ of 5.358, which only has an error of 0.075% compared with the NHT prediction. Fig. 7 shows the CNN predictions for all accepted successful swaps and the NHT evaluation of the same structures.

The CNN is able to accurately predict the $\bar{k}_{\rm eff}$ at each iteration. The predicted change of $\bar{k}_{\rm eff}$ with iteration by CNN follows a similar pattern to that of the NHT. The MAPE between the NHT and CNN models prediction for all successful swaps is 1.1%, which is worse than the reported testing MAPE from Table 5. But the higher MAPE is expected due to the random nature of structures resulting from voxel swapping. This trend can be confirmed from Fig. 7: the NHT and CNN predictions agree at both low and high $\bar{k}_{\rm eff}$ values, with a bulge of disagreement in the middle of the domain, where the structures resemble random distributions of voxels.

In this topology optimization case the NHT simulation averages 34.2 s per iteration (from Table 1), and the CNN averages 15 ms per iteration on a commercial GPU. The CNN based optimization is 2280 times faster per iteration, which saves over 9,495 h in the span of one million iterations.

5.2. Case B: k_{eff} in the x-direction, $\bar{k}_s = 341.7$ (Aluminum-water)

Effective properties of the aluminum-water system predicted by CNN, as seen in Section 4, have considerably higher errors than the case with the thermal conductivity ratio of 10. The ratio of thermal conductivities is close to other metals filled with fluids, so this is a case with more real applications. If the topology optimization using CNN correctly predicts the trend in thermal conductivity in the aluminum-water system with changes to the structure, then this modeling tool can be extrapolated to other material combinations.

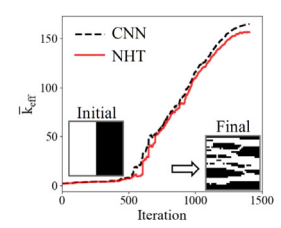


Fig. 8. Evolution of the $\bar{k}_{\rm eff}$ from topology optimization, comparing the NHT and CNN predictions for every step, along with initial and final structures.

In this case, 1406 iterations were successful, and 743 mutations occurred. The final image, displayed in Fig. 8 has a $\bar{k}_{\rm eff}$ of 156.43 according to the NHT model, while the CNN predicts the ratio to be 164.81, which is 5.36% higher than the NHT model. The theoretical maximum according to Eq. (12) is 171.35. Hence the NHT prediction shows the optimized structure achieved a $\bar{k}_{\rm eff}$ within 9.12% from the theoretical maximum. The evolution of $\bar{k}_{\rm eff}$ with successful voxel swaps is displayed in Fig. 8, with the NHT results for every structure also included for comparison.

Throughout the optimization, the CNN and NHT follow the same general trend, which confirms that the CNN model correctly predicts increases in the $\bar{k}_{\rm eff}$. CNN predictions' MAPE relative to NHT results was 11.84% on the successful iterations. The relative increase in MAPE compared to case A is similar to what is observed through validation in Section 4. The increase in error from testing, similar to Section 5.1, is attributed to intermediate structures that are a natural outcome of random voxel swapping. As stated before, the regular shapes packed in the majority of the training dataset are there to simulate realistic structures. It is noteworthy that besides the reported accuracy, in both cases A and B, the CNN and NHT models agree better at the initial state and near the converged state, as seen in Fig. 8. Near the initial and converged states, the structures are better connected and more resembling the training data.

With $\bar{k}_s=341.7$, the NHT simulation averages 371.2 s per iteration (from Table 1). The CNN prediction time is not dependent on \bar{k}_s , and still averages 15 ms per iteration on a commercial GPU. The CNN based optimization is 24,746 times faster per iteration, which saves over 103,105 h in the span of one million iterations.

5.3. Case C: k_{eff} in both x and y directions, $\bar{k}_s = 10$

This case simultaneously optimizes $\bar{k}_{\rm eff}$ for the x and y directions, with a cost function defined in Eq. (14):

$$cost = \bar{k}_{eff,x} + \bar{k}_{eff,y} - |\bar{k}_{eff,x} - \bar{k}_{eff,y}|$$

$$(14)$$

The cost function includes the effective thermal conductivities in the x-direction, $\bar{k}_{\rm eff,y}$, and y-direction, $\bar{k}_{\rm eff,y}$. The simulation only considers the thermal conductivity ratio of 10. The absolute difference between

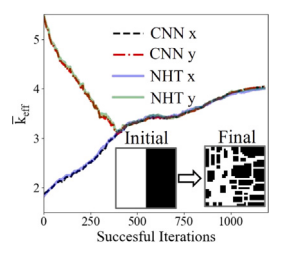


Fig. 9. Evolution of the $\bar{k}_{eff,x}$ and $\bar{k}_{eff,y}$ from topology optimization, comparing the NHT and CNN predictions for every step, along with the final structure generated.

 $ar{k}_{\mathrm{eff,y}}$ and $ar{k}_{\mathrm{eff,y}}$ is added to the cost function such that the algorithm does not maximize one of the properties to the detriment of the other, thus avoiding local maxima outcomes. The penalizing term ensures that $ar{k}_{\mathrm{eff,y}}$ and $ar{k}_{\mathrm{eff,y}}$ will always be similar through the CNNs prediction, thus ensuring $ar{k}_{\mathrm{eff}}$ of the structure is an isotropic property in the 2D plane.

Within the one million swaps attempted, 1180 of them were successful, and 593 mutations occurred. The final structure can be seen in Fig. 9, along with the comparison of NHT and CNN predictions for $\bar{k}_{\rm eff,y}$ and $\bar{k}_{\rm eff,y}$. The cost function of the final structure predicted by the CNN is 8.08. In comparison, the cost function simulated by the NHT model is 8.02 for the final structure.

When using a GPU, the CNN model can evaluate both images (x and y direction) simultaneously, hence taking the same time as evaluating one image alone, and additional advantage of the CNN model. In the entire domain, the CNN model has a MAPE of 0.67% compared to the NHT model, with trends similar to the ones seen in Fig. 7.

With $\bar{k}_{\rm s}=10$, the NHT simulation averages 34.2 s per iteration, and the CNN averages 15 ms per iteration on a commercial GPU. However in this case the NHT has to simulate both x and y directions independently, hence taking twice as long. Because modern GPUs can take batches of images, even a commercial GPU takes the same amount of time to evaluate both x and y directions simultaneously. Therefore, GPU-based estimation is 4560 times faster per iteration, which saves over 18,990 h in the span of one million iterations.

5.4. Case D: k_{eff} in the x-direction, $\bar{k}_s = 10$, and surface area

Surface area is an important parameter in energy related heterogeneous systems. This case study is meant to showcase how the output of the CNN can be used alongside another variable which does not have the same units for optimization. The first step in combining thermal conductivity and surface area is normalizing and non-dimensionalizing both quantities.

Since $\bar{k}_{\rm eff,parallel}$ represents the maximum possible $\bar{k}_{\rm eff}$ and $\bar{k}_{\rm eff,series}$ represents the minimum, for a given porosity, ϵ , and a thermal conductivity ratio, $\bar{k}_{\rm s}$, $\bar{k}_{\rm eff}$ is normalized by Eq. (15).

$$\bar{k}_{\rm eff,norm} = \frac{\bar{k}_{\rm eff} - \bar{k}_{\rm eff,series}}{\bar{k}_{\rm eff,parallel} - \bar{k}_{\rm eff,series}} \tag{15}$$

While it seems natural to use $\bar{k}_{\rm eff,norm}$ as the output of the CNN instead of training it for multiple values of $\bar{k}_{\rm s}$, for any given structure, $\bar{k}_{\rm eff,norm}$ does change with the ratio of $\bar{k}_{\rm s}$. Currently there is no way to extrapolate $\bar{k}_{\rm eff,norm}$ from one thermal conductivity ratio to all ratios. Appendix C briefly explores the issues with using $\bar{k}_{\rm eff,norm}$ as the network output.

For the surface area, a similar equation is proposed in Eq. (16), where the maximum surface area, $SA_{\rm max}$, for a porosity of $\epsilon=0.5$ is a perfect checkerboard pattern, and the minimum, $SA_{\rm min}$, is a configuration such as the parallel or series configurations from Fig. 3, where all voxels of any given phase are clumped together. SA is also normalized, using Eq. (16).

$$\bar{SA} = \frac{SA - SA_{\min}}{SA_{\max} - SA_{\min}} \tag{16}$$

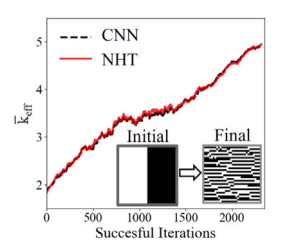


Fig. 10. Evolution of the $\bar{k}_{\rm eff}$ from topology optimization, comparing the NHT and CNN predictions for every step. The final structure is also compared to the original image.

The cost function is then expressed in Eq. (17), where the terms w_k and w_{SA} are weights introduced to regulate which parameter the topology optimization algorithm prioritizes. In this study both variables are assigned equal importance, so $w_k = w_{SA} = 1$.

$$cost = w_k \bar{k}_{eff,norm} + w_{SA} \bar{SA}$$
 (17)

From the one million attempted voxel swaps, using $\bar{k}_{\rm s}=10,\,2,319$ iterations were successful and 1349 mutations occurred. The $\bar{k}_{\rm eff}$ predicted by the CNN is 4.93 and simulated by the NHT model it is 4.95. The error in CNN prediction relative to the NHT model is 0.4% for the final image, displayed in Fig. 10. The MAPE in prediction, from data shown in Fig. 10, is 0.88%, slightly better than what was displayed in case A. The NHT calculated $\bar{k}_{\rm eff}$ for the final structure is 10% off from the theoretical maximum of 5.5, while $S\bar{A}$ from Eq. (16) is 0.467.

The results from this study are better put into perspective when compared to the results displayed in Fig. 7, in which the same conditions for x-direction thermal conductivity were optimized but without any constraint to the surface area. It is clear by visually comparing Figs. 7 and 10 that the latter presents a much larger surface area, while the $\bar{k}_{\rm eff}$ is only 3.8% lower. Holding similar weighing factors for the surface area and $\bar{k}_{\rm eff}$ in the cost function in Eq. (17) penalizes the optimization algorithm to move a pixel with a large surface area for a minimal increase in $\bar{k}_{\rm eff}$. The CNN maintained the ability to correctly predict trends in $\bar{k}_{\rm eff}$ for structures with high surface areas and optimize the cost function.

With $\bar{k}_s = 10$, the NHT simulation averages 34.2 s per iteration, and the CNN averages 15 ms per iteration on a commercial GPU. The time taken to evaluate surface area is negligible in both cases. Therefore, the speedup observed here is the same as Section 5.1.

6. Conclusion

The proposed model provides an on-demand alternative to estimating effective thermal conductivity on a system with two phases without any compromises or simplifications to the geometry of the system. The trained networks at four different ratios of thermal conductivity among the two phases are simple to use and produce results orders of magnitude faster than NHT simulations. The model is also capable of extrapolating from the learned data to new structures, as seen in the case of topology optimization through voxel swapping. In that case, the intermediate structures do not appear realistic and were not directly encoded in training, yet the model retains reasonable consistency and accuracy in prediction.

Through the studies presented, we determined that the two main sources of error are the NHT model used to evaluate the training dataset and the diversity of the dataset. Thus, the main restriction of creating highly efficient and accurate CNNs to predict properties, such as effective diffusivity, structural properties, effective permeability, average pore size, and surface area, among others, is the creation of a diverse and accurate training datasets. The training of the CNN itself is minuscule in terms of computational time compared to creating a large dataset. The full dataset used in this study [25], the models trained on

the four different thermal conductivity ratios, as well as example code to use the trained models, are available to the reader.

One critical limitation of the CNN model is that it is completely blind to physics, and does not produce a temperature or heat flux map of the domain as an output. In that sense, CNN cannot be paired with the Evolutionary Structural Optimization (ESO) [40] approach, which is a powerful method for taking educated guesses at potential voxel swaps in the structural optimization field. The CNN model can be improved by taking physical properties in addition to images, as input. In that case, the model would be able to generalize to a wider variety of material combinations at the cost of increased computational time.

Nonetheless, the efficiency and accuracy displayed by the CNN are attractive for both academic and industrial design of heterogeneous materials and on demand effective thermal conductivity estimation. Furthermore, this study shows that the accuracy and generalizability of the training dataset attribute to the majority of errors on CNN predictions. Thus, future research directions of the CNN model include increasing the size and improving the quality of the training dataset, adapting the model to three dimensions, and extending the model to other materials with different properties.

Declaration of competing interest

The authors declare that they have no known competing financial interests or personal relationships that could have appeared to influence the work reported in this paper.

Data availability

The data will be publicly available.

Acknowledgments

A. A. and X. L. highly appreciate the funding support from National Science Foundation, USA (Award: 1941083) and NASA EPSCoR, USA (Award: 80NSSC22M0221).

This work was only possible with the Extreme Science and Engineering Discovery Environment (XSEDE), USA grants for computational time in the Bridges2 and Expanse supercomputers, under the awards MAT210007 and MAT210014.

Appendix A. Dataset details

Often, there is a strong correlation between porosity/solid volume fraction (SVF) and $\bar{k}_{\rm eff}$. Also, for any image generated, the $k_{\rm eff}$ is bound to stay between the theoretical maximum and the theoretical minimum. With these two key ideas in mind, the dataset was specifically designed to cover as diverse of a $\bar{k}_{\rm eff}$ as possible. Fig. A.11 below contains more details.

By comparing Fig. A.11 (a) and (b), it becomes evident how it is not only beneficial to augment the dataset in terms of encoding additional information, but also by flipping the color scheme of the images the augmented dataset has a more symmetrical distribution of SVF.

Note on Fig. A.11 (c) the design space of \bar{k}_{eff} as a function of SVF and how it is bounded by the theoretical cases. Near the edges (SVF close to 0 or 1), fewer images are needed since the theoretical maximum and minimum converge to the same value. On the other hand, between SVF of 0.3 and 0.7 is where the majority of images need to be to cover the design space.

Finally, from Fig. A.11 (c) we observe that the theoretical cases used for validation were not encoded in training and are not part of this dataset. Otherwise the red dots would overlap with the dashed black line.

Appendix B. Finite volume and LBM comparison

From the results presented in Fig. 3, the deviation from the NHT simulation and the analytical results is negligible for ratios of thermal conductivity less than 10^4 . Above that number, we note an increase in error for the series structures, while the parallel structures still present little to no error, as already discussed.

For comparison, Zhu et al. [33] utilizes similar theoretical test cases in 3D to validate a conventional LBM as well as a modified one in 3D for effective thermal conductivity. While numerical comparisons between LBM and theoretical cases are not explicitly expressed, by visual inspection we note significant differences between the models and theoretical results, especially the convectional LBM.

Ke et al. [32] proposed another modified LBM method for 2D effective thermal conductivity estimation. For the same theoretical test cases, with thermal conductivity ratios varying between 0.01 and 100, the authors reported deviations of less than 1.0% for both parallel and series test cases. For these thermal conductivity ratios, our error is less than 0.01% with the convergence criteria used in the training dataset.

Neither study has additional data and results published in open access format, so we refrain from further comparisons. However, we do note that a version of our NHT simulation for effective thermal conductivity, both in 2D and 3D, is available on GitHub.² The entire dataset and all simulation results used to train the CNNs are also available [25] to facilitate comparisons.

Regarding the NHT model, several mechanisms can augment accuracy, such as mesh refinement, convergence criteria, and the prescribed cutoff iterations for the iterative solver. However, considering the foundational framework of this study involves the execution of hundreds of thousands of simulations, the determination of convergence criteria and the establishment of a maximum iteration count were strategic

² https://github.com/adama-wzr/Keff-CFD

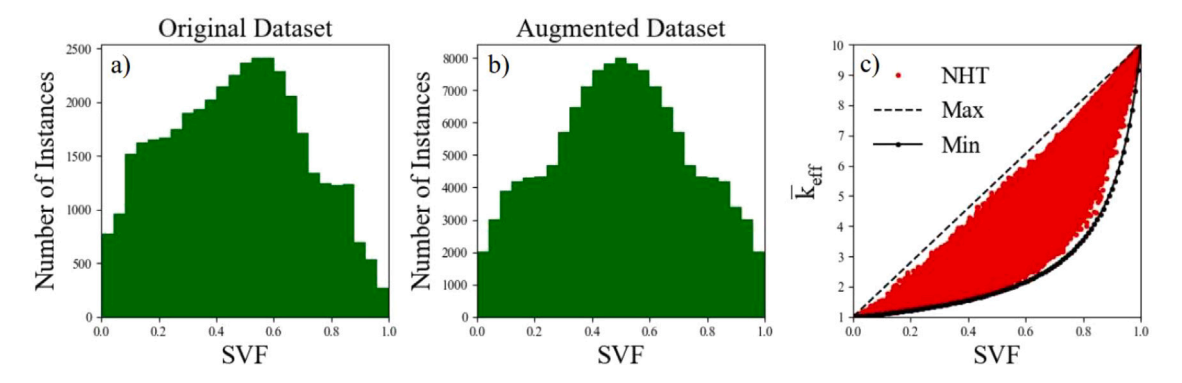


Fig. A.11. (a) shows a histogram of the SVF distribution of the original 40,000 images. (b) shows the same histogram but for the augmented dataset of 130,000 images. c() Compares the $\bar{k}_{\rm eff}$ as a function of SVF for the entire augmented dataset.

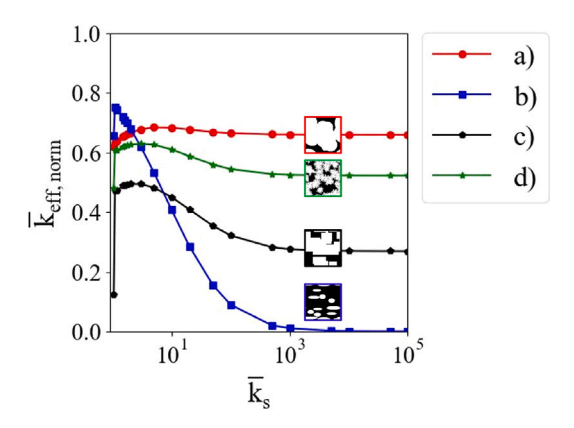


Fig. C.12. Evolution of $\bar{k}_{\rm eff,norm}$ as a function of $\bar{k}_{\rm s}$.

choices aimed at achieving precise solutions within a practical time frame. Hence those were fixed values for all simulations and comparisons to the theoretical model. Thus, to increase the accuracy, we recommend simply increasing the maximum number of iterations and making the convergence criteria more strict. Through testing, we have observed that this adjustment significantly decrease the error versus the theoretical model at the cost of computational time.

Appendix C. k_{eff} Normalization issues

The normalized form of $\bar{k}_{\rm eff,norm}$, from Eq. (15), is a convenient way of expressing the effective thermal conductivity. For a given porosity, $\bar{k}_{\rm eff,norm}$ is a measure between 0 and 1, respectively representing the maximum and minimum theoretical effective thermal conductivity. However, as we will shown in this section, the variable $\bar{k}_{\rm eff,norm}$ is still a function of $\bar{k}_{\rm s}$, and no equations currently exist to fit the curves of $\bar{k}_{\rm eff,norm}$ as a function of $\bar{k}_{\rm s}$ and ϵ for a given geometry.

For this study, consider the geometries presented shown in Fig. 1. The porosities are 0.20, 0.75, 0.38, and 0.33 respectively. The values of \bar{k}_s vary between $\bar{k}_s = 1.05$ and 10^5 . For each geometry and \bar{k}_s , the maximum and minimum are calculated according to Eqs. (11) and (12) respectively. Finally, the value of $\bar{k}_{\rm eff}$ is calculated using the NHT algorithm outlined in Section 2. The results are shown in Fig. C.12.

Figs. 1c and 1d have similar porosities, yet, as seen in C.12, it is not obvious how the curves behave and what variables best fit the curve. Curve (b) peaks around $\bar{k}_{\rm S}=2$, curve (c) peaks around $\bar{k}_{\rm S}=5$, while curves (a) and (d) peak around $\bar{k}_{\rm S}=10$. Curve (b), as $\bar{k}_{\rm S}$ increases, converges to 0, while all other curves converge to their own number. In addition, curve (b) peaks the highest, and converges to the lowest value out of the ones presented.

Currently, there is no research discussing what variables define these curves other than porosity and the ratio of thermal conductivities. Having the ability to infer $\bar{k}_{\rm eff}$ for any $\bar{k}_{\rm s}$ for a given geometry from only one simulation would also allow for one CNN to predict $\bar{k}_{\rm eff,norm}$ for all combinations of thermal conductivity ratios. That is currently not the case, which is a major reason why we define $\bar{k}_{\rm eff}$ and train the CNN for four different ratios of $\bar{k}_{\rm s}$.

References

- [1] Wu X, Zhu Y. Heterogeneous materials: A new class of materials with unprecedented mechanical properties. Mater Res Lett 2017;5(8):527–32. http://dx.doi.org/10.1080/21663831.2017.1343208.
- [2] Lin G, Liu S, Qu G, Song Y, Li T, Liu F, et al. Effect of pore size distribution in the gas diffusion layer adjusted by composite carbon black on fuel cell performance. Int J Energy Res 2021;45(5):7689–702. http://dx.doi.org/10.1002/er.6350, URL https://onlinelibrary.wiley.com/doi/full/10.1002/er.6350.
- [3] Cui CL, Schweich D, Villermaux J. Influence of pore diameter distribution on the determination of effective diffusivity in porous particles. Chem Eng Process 1989;26(2):121–6. http://dx.doi.org/10.1016/0255-2701(89)90004-4.

- [4] Liu X, Song F, Xu Q, Luo Q, Tian Y, Li J, et al. The influence of pore size distribution on thermal conductivity, permeability, and phase change behavior of hierarchical porous materials. Sci China Technol Sci 2021;64(11):2485–94. http://dx.doi.org/10.1007/s11431-021-1813-0.
- [5] Tian S, Ren W, Li G, Yang R, Wang T. A theoretical analysis of pore size distribution effects on shale apparent permeability. Geofluids 2017;2017. http: //dx.doi.org/10.1155/2017/7492328.
- [6] Bhattacharjee B. Influence of pore size distribution on the properties of a stabilized soil cement system. In: Geo-China 2016. American Society of Civil Engineers; 2016, p. 53–60. http://dx.doi.org/10.1061/9780784480069.007, URL https://ascelibrary.org/doi/10.1061/9780784480069.007.
- [7] Ranut P. On the effective thermal conductivity of aluminum metal foams: Review and improvement of the available empirical and analytical models. Appl Therm Eng 2016;101:496–524. http://dx.doi.org/10.1016/j.applthermaleng. 2015.09.094.
- [8] Wang F, Li X. The stagnant thermal conductivity of porous media predicted by the random walk theory. Int J Heat Mass Transfer 2017;107:520–33. http: //dx.doi.org/10.1016/j.ijheatmasstransfer.2016.11.069.
- [9] Wang F, Li X, Tan J, Hao X, Xiong B. Pore-scale prediction of the oxygen effective diffusivity in porous battery electrodes using the random walk theory. Int J Heat Mass Transfer 2022;183:122085. http://dx.doi.org/10.1016/j.ijheatmasstransfer. 2021.122085.
- [10] Fukushima K. Biological cybernetics neocognitron: A self-organizing neural network model for a mechanism of pattern recognition unaffected by shift in position. Biol Cybern 1980;36:202.
- [11] Minaee S, Boykov YY, Porikli F, Plaza AJ, Kehtarnavaz N, Terzopoulos D. Image segmentation using deep learning: A survey. IEEE Trans Pattern Anal Mach Intell 2021. http://dx.doi.org/10.1109/TPAMI.2021.3059968, arXiv:2001.05566.
- [12] Yang Z, Yabansu YC, Al-Bahrani R, keng Liao W, Choudhary AN, Kalidindi SR, et al. Deep learning approaches for mining structure-property linkages in high contrast composites from simulation datasets. Comput Mater Sci 2018;151(April):278–87. http://dx.doi.org/10.1016/j.commatsci.2018.05.014.
- [13] Cecen A, Dai H, Yabansu YC, Kalidindi SR, Song L. Material structure-property linkages using three-dimensional convolutional neural networks. Acta Mater 2018;146:76–84. http://dx.doi.org/10.1016/j.actamat.2017.11.053.
- [14] Wu H, Fang WZ, Kang Q, Tao WQ, Qiao R. Predicting effective diffusivity of porous media from images by deep learning. Sci Rep 2019;9(1):1–12. http://dx.doi.org/10.1038/s41598-019-56309-x, URL https://www.nature.com/ articles/s41598-019-56309-x.
- [15] Krizhevsky A, Sutskever I, Hinton GE. ImageNet classification with deep convolutional neural networks. Commun ACM 2017;60(6):84–90. http://dx.doi.org/10.1145/3065386, URL http://code.google.com/p/cuda-convnet/.
- [16] He K, Zhang X, Ren S, Sun J. Deep residual learning for image recognition. In: Proceedings of the IEEE computer society conference on computer vision and pattern recognition, vol. 2016-Decem. IEEE Computer Society; 2016, p. 770–8. http://dx.doi.org/10.1109/CVPR.2016.90, arXiv:1512.03385.
- [17] Wei H, Zhao S, Rong Q, Bao H. Predicting the effective thermal conductivities of composite materials and porous media by machine learning methods. Int J Heat Mass Transfer 2018;127:908–16. http://dx.doi.org/10.1016/j.ijheatmasstransfer. 2018.08.082.
- [18] Zhu MX, Song HG, Yu QC, Chen JM, Zhang HY. Machine-learning-driven discovery of polymers molecular structures with high thermal conductivity. Int J Heat Mass Transfer 2020;162. http://dx.doi.org/10.1016/j.ijheatmasstransfer. 2020.120381.
- [19] Wei H, Bao H, Ruan X. Perspective: Predicting and optimizing thermal transport properties with machine learning methods. Energy AI 2022;8. http://dx.doi.org/ 10.1016/j.egyai.2022.100153.
- [20] Simonyan K, Zisserman A. Very deep convolutional networks for large-scale image recognition. In: 3rd international conference on learning representations, ICLR 2015 - conference track proceedings. 2015, p. 1–14, arXiv:1409.1556.
- [21] Bendsøe MP. Optimization of structural topology, shape, and material. Berlin Heidelberg: Springer; 1995, http://dx.doi.org/10.1007/978-3-662-03115-5.
- [22] Sevart CD, Bergman TL. An itertive design method to reduce the overall thermal resistance in a conjugate conduction-free convection configuration. Front Heat Mass Transf 2019;13. http://dx.doi.org/10.5098/hmt.13.18.
- [23] Sevart CD, Bergman TL. Evolutionary design method for a conducting solid cooled by combined free convection and radiation. J Heat Transfer 2021;143(4):1–9. http://dx.doi.org/10.1115/1.4049841.
- [24] Ding R, Zhang S, Chen Y, Rui Z, Hua K, Wu Y, et al. Application of machine learning in optimizing proton exchange membrane fuel cells: A review. Energy AI 2022;9:100170. http://dx.doi.org/10.1016/j.egyai.2022.100170.
- [25] Adam A, Li X, Fang H. 2D binary images and effective thermal conductivity CFD results. Mendeley; 2023, http://dx.doi.org/10.17632/454DSRMDYF.1, URL https://data.mendeley.com/datasets/454dsrmdyf/1.
- [26] Bargmann S, Klusemann B, Markmann J, Schnabel JE, Schneider K, Soyarslan C, et al. Generation of 3D representative volume elements for heterogeneous materials: A review. Prog Mater Sci 2018;96:322–84. http://dx.doi.org/10.1016/j.pmatsci.2018.02.003.

- [27] Bostanabad R, Zhang Y, Li X, Kearney T, Brinson LC, Apley DW, et al. Computational microstructure characterization and reconstruction: Review of the state-of-the-art techniques. Prog Mater Sci 2018;95:1–41. http://dx.doi.org/10. 1016/j.pmatsci.2018.01.005.
- [28] Ju Y, Huang Y, Zheng J, Qian X, Xie H, Zhao X. Multi-thread parallel algorithm for reconstructing 3D large-scale porous structures. Comput Geosci 2017;101(June 2016):10–20. http://dx.doi.org/10.1016/j.cageo.2017.01.003.
- [29] Adam A, Wang F, Li X. Efficient reconstruction and validation of heterogeneous microstructures for energy applications. Int J Energy Res 2022. http://dx.doi. org/10.1002/er.8578, URL https://onlinelibrary.wiley.com/doi/full/10.1002/er. 8578.
- [30] Politis MG, Kikkinides ES, Kainourgiakis ME, Stubos AK. A hybrid process-based and stochastic reconstruction method of porous media. Microporous Mesoporous Mater 2008;110(1):92–9. http://dx.doi.org/10.1016/J.MICROMESO. 2007.09.024.
- [31] Wang M, Wang J, Pan N, Chen S. Mesoscopic predictions of the effective thermal conductivity for microscale random porous media. Phys Rev E 2007;75(3). http://dx.doi.org/10.1103/PhysRevE.75.036702, URL https://escholarship.org/ uc/item/7891j8jt.
- [32] Ke X, Duan Y. A spatially-varying relaxation parameter Lattice Boltzmann Method (SVRP-LBM) for predicting the effective thermal conductivity of composite material. Comput Mater Sci 2019;169. http://dx.doi.org/10.1016/j.commatsci. 2019.109080.
- [33] Zhu W, Kan A, Chen Z, Zhang Q, Zhang J. A modified Lattice Boltzmann method for predicting the effective thermal conductivity of open-cell foam materials. Int Commun Heat Mass Transfer 2022;133:105957. http://dx.doi.org/10.1016/j. icheatmasstransfer.2022.105957.

- [34] Yang L, Shami A. On hyperparameter optimization of machine learning algorithms: Theory and practice. Neurocomputing 2020;415:295–316. http://dx.doi.org/10.1016/j.neucom.2020.07.061, arXiv:2007.15745.
- [35] Goodfellow JJ, Bulatov Y, Ibarz J, Arnoud S, Shet V. Multi-digit number recognition from street view imagery using deep convolutional neural networks. In: 2nd international conference on learning representations, ICLR 2014 conference track proceedings. International Conference on Learning Representations, ICLR; 2014, http://dx.doi.org/10.48550/arxiv.1312.6082, arXiv:1312.6082, URL https://arxiv.org/abs/1312.6082v4.
- [36] Li X, Zhang Y, Zhao H, Burkhart C, Brinson LC, Chen W. A transfer learning approach for microstructure reconstruction and structure-property predictions. Sci Rep 2018;8(1):1–13. http://dx.doi.org/10.1038/s41598-018-31571-7, arXiv: 1805.02784, URL http://dx.doi.org/10.1038/s41598-018-31571-7.
- [37] Smith SL, Kindermans PJ, Ying C, Le QV. Don't decay the learning rate, increase the batch size. In: 6th international conference on learning representations, ICLR 2018 - conference track proceedings. 2018, arXiv:1711.00489.
- [38] Kingma DP, Ba JL. Adam: A method for stochastic optimization. In: 3rd international conference on learning representations, ICLR 2015 - conference track proceedings. 2015, arXiv:1412.6980.
- [39] Kirkpatrick S, Gelatt CD, Vecchi MP. Optimization by simulated annealing. Science 1983;220(4598):671–80. http://dx.doi.org/10.1126/science.220.4598.
- [40] Xie Y, Steven G. A simple approach to structural optimization. Computers Struct 1993;49(5):885–96.